Calphad 64 (2019) 55–65

Contents lists available at ScienceDirect

Calphad

journal homepage: www.elsevier.com/locate/calphad

Phase diagrams and elastic properties of the Fe-Cr-Al alloys: A first-principles based study

Ruirui Wang[a,b], Xiao Zhang[a,b], Huaiyu Wang[a,b], Jun Ni[a,b,*]

[a] State Key Laboratory of Low-Dimensional Quantum Physics, Department of Physics, Tsinghua University, Beijing 100084, People's Republic of China
[b] Collaborative Innovation Center of Quantum Matter, Beijing 100084, People's Republic of China

ARTICLE INFO

MSC:
82B26
74A15
81–04

Keywords:
Ternary alloy system
Phase diagrams
Elastic properties
First-principles calculations

ABSTRACT

The phase diagrams and elastic properties of the Fe-Cr-Al alloys in full-temperature and all-compositional ranges are calculated. By combining first-principles calculations and cluster variation method, binary and ternary phase diagrams are obtained. A new ternary ordered phase B32 which is different from ternary extension of binary phases appears in the ternary section around temperature of 600 K. The binary FeAl phases show an extremely high solubility for Cr, while the binary CrAl phase solid solution has a low solubility for Fe. By combining first-principles calculations and cluster expansion method, the bulk modulus, shear modulus and Poisson's ratio are calculated. The shear modulus and Poisson's ratio show a strong ordering dependency, while the ordering dependency in bulk modulus is weak. Disordered Fe-Cr alloys with a little Al solvent shows ductile property, the Al-rich corner has brittle property.

1. Introduction

Fe-Cr-Al alloys are of interest in high temperature structural applications [1] due to the easy production of protective coatings alumina [2,3]. They have also been proposed as candidates for nuclear-grade alloys [4,5]. Besides the extraordinary corrosion and oxidation resistance [6,7], the properties such as formability, mechanical strength [8,9], creep strength [10], and radiation tolerance [11] have been investigated.

The bulk modulus, shear modulus and Poisson's ratio are three most fundamental mechanical properties. The bulk modulus and shear modulus reflect the resistance of a material against shape and shear deformation [12], and Poisson's ratio characterizes different mechanical behavior such as stiff and brittle [13,14]. The first-principles calculations of elastic properties on binary Fe-Al alloys [15,16], Fe-Cr alloys [17,18] and CrAl-B2 phase [19] revealed the lattice, pressure and concentration dependencies of the three properties. The first-principles based calculations present a reduction in bulk modulus as the increase of temperature in the CrAl-B2 and FeTi-B2 phase [19,20]. Due to the complexity of ternary alloys, there are no first-principles calculations of mechanical properties on Fe-Cr-Al alloys.

Phase diagrams are the foundation in performing materials research. Calculations of phase diagrams are of great interest since they serve as a roadmap for materials design and process optimization. The experimental phase diagram of the Fe-Cr-Al alloys has two sections, the Fe-Cr rich section in which Fe-Cr solid solution is stable [21] and the Al rich section in which ternary intermetallic phases exist [22]. At 1000 °C, no ternary intermetallic phase was found experimentally in the Al-corner region [23]. The binary intermetallic phases can be extended to ternary ones by dissolving considerable amounts of the third component. In the exploration of Fe-Cr-Al quasicrystals, ternary intermetallic phases which were crystal approximations of quasicrystals in Al-rich regions were experimentally sythesised [24–27]. Although there are phase diagrams of the Fe-Cr-Al alloys obtained by the experimental methods and thermodynamic approach [28,29], there are no phase diagrams based on first-principles calculations.

In this paper, we have calculated the phase diagrams and elastic properties of the Fe-Cr-Al system in full-temperature and all-compositional ranges based on first-principles calculations. We found that Fe-Cr-Al system shows a high solubility for Cr and low solubility for Fe, and a new ternary ordered phases B32 is found around 600 K. There are strong ordering dependencies in the shear modulus and Poisson's ratio, and Poisson's ratio reveals the brittle properties in Al-rich corner. The outline of this paper is as follows: Section 2 describes the methods used for the calculations. Section 3 shows the results on phase diagrams and elastic properties. And Section 4 is our conclusions.

* Corresponding author at: State Key Laboratory of Low-Dimensional Quantum Physics, Department of Physics, Tsinghua University, Beijing 100084, People's Republic of China.
E-mail address: junni@mail.tsinghua.edu.cn (J. Ni).

https://doi.org/10.1016/j.calphad.2018.11.010
Received 16 August 2018; Received in revised form 16 November 2018; Accepted 16 November 2018
Available online 04 December 2018

2. Methods

The Fe-Cr-Al phase diagrams and elastic properties are investigated in the following way. The first-principles calculations give the stable phases and elastic properties at zero temperature. Then the results are extended to finite temperature by means of the cluster variation method (CVM) [30,31] and cluster expansion method(CEM) [32]. In the following, first-principles calculations, CVM and CEM are briefly introduced.

2.1. First-principles calculations

The formation energies and elastic properties of the stoichiometric compounds are calculated using VASP(the Vienna ab initio simulation package) [33,34]. The approach is based on an iterative solution of the Kohn-Sham equations of the density-functional theory (DFT). Since the system is known to be magnetic, we have performed the spin-polarized calculations. The ion core are modeled by the projector augmented wave potentials (PAW) [35]. The valence electrons are described by a plane-wave basis set with cutoff energy of 520 eV and the exchange correlation functional of the generalized gradient approximation (GGA) is given by Perdew et al [36]. The tolerance of the energy convergence is 10^{-5} eV. In order to determine the accurate interaction parameters, we have employed the same size of supercells for different structures [37]. The calculations are performed on the supercell of same size with the $D0_3$ structure containing 16 atoms. A mesh of Γ centered grids $10 \times 10 \times 10$ is used to sample the Brillouin zone for self-consistent calculations.

2.2. Cluster variation method

The cluster variation method(CVM) introduced by Kikuchi [31] has been widely used in investigating alloy phase diagrams [38–40]. For the phase diagram calculations of Fe-Cr-Al alloy, the irregular tetrahedron (IT) cluster approximation [41] which is commonly used in literature [39,40,60] is adopted. Fig. 1 is the IT cluster and the four vertices of an IT cluster are labeled by i, j, k, l for convenience. The basic variables in CVM are the occupation probabilities on sublattices of the basic IT cluster. Point probability p_α^i represents species α occupying site i, pair probability $p_{ij}^{\alpha\beta}$ represents species α and β occupying sites i and j respectively, three-point probability $p_{ijk}^{\alpha\beta\gamma}$ represents species α, β and γ occupying sites i, j and k respectively and four-point probability $p_{\alpha\beta\gamma\delta}^{ijkl}$ represents species α, β, γ and δ occupying sites i, j, k and l, respectively. In our calculations, we consider only effective interaction energies containing nearest neighbor, next neighbor, three-body and four-body interactions. The largest correlations in entropy is four-body correlation and vibrational effects on the thermodynamics are neglected here.

The grand potential J of an n-element alloys with N lattice points is written as [41,42]

$$J = U - TS - N\sum_{\alpha=1}^{n}\mu_\alpha x_\alpha. \tag{1}$$

The first term U is the formation energy, which can be represented as

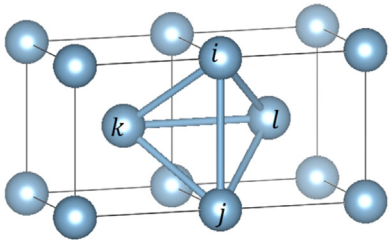

Fig. 1. Irregular tetrahedron cluster on bcc lattice.

$$U = 6N\sum_{\alpha\beta\gamma\delta}\varepsilon_{\alpha\beta\gamma\delta}p_{\alpha\beta\gamma\delta}^{ijkl}, \tag{2}$$

where $\varepsilon_{\alpha\beta\gamma\delta}$ is the effective four-body interaction parameter [43], which can be written as

$$\varepsilon_{\alpha\beta\gamma\delta} = \frac{1}{6}(w_{\alpha\gamma}^{(1)} + w_{\alpha\delta}^{(1)} + w_{\beta\gamma}^{(1)} + w_{\beta\delta}^{(1)}) + \frac{1}{4}(w_{\alpha\beta}^{(2)} + w_{\gamma\delta}^{(2)}) + \tilde{w}_{\alpha\beta\gamma\delta}. \tag{3}$$

The $w_{\alpha\gamma}^{(1)}$ s are interactions between the nearest neighbors and $w_{\alpha\beta}^{(2)}$ s are those between the next nearest neighbors. The $\tilde{w}_{\alpha\beta\gamma\delta}$ s are the correction terms beyond two-body interactions in the tetrahedron approximation [43,44]. These interactions are deduced from formation energies of stoichiometric compounds obtained by the first-principles calculations [37]. In the second term of Eq. (1), T is temperature and S is the configurational entropy [45]. In the third term of Eq. (1), μ_α and x_α are respectively the chemical potential and concentration of species α. The latter can be calculated by the point probabilities p_i^α as

$$x_\alpha = (p_\alpha^i + p_\alpha^j + p_\alpha^k + p_\alpha^l)/4. \tag{4}$$

By minimize the normalized grand potential $\frac{J}{k_BTN}$ with respect to the probability $p_{ijkl}^{\alpha\beta\gamma\delta}$, we obtain the natural iteration method (NIM) formula [44,45]

$$p_{\alpha\beta\gamma\delta}^{ijkl} = \Phi\frac{\left(p_{\alpha\beta\gamma}^{jkl}p_{\alpha\beta\delta}^{ijl}p_{\alpha\gamma\delta}^{ikl}p_{\beta\gamma\delta}^{jkl}\right)^{\frac{1}{2}}\left(p_\alpha^i p_\beta^j p_\gamma^k p_\delta^l\right)^{\frac{1}{24}}}{\left(p_{\alpha\beta}^{ij}p_{\gamma\delta}^{kl}\right)^{\frac{1}{4}}\left(p_{\alpha\gamma}^{ik}p_{\alpha\delta}^{il}p_{\beta\gamma}^{jk}p_{\beta\delta}^{jl}\right)^{\frac{1}{6}}}, \tag{5}$$

where the factor Φ depends on the interaction energies and chemical potentials

$$\Phi = \exp\left[-\frac{\varepsilon_{\alpha\beta\gamma\delta}}{k_BT} + \frac{1}{24k_BT}(\mu_\alpha + \mu_\beta + \mu_\gamma + \mu_\delta) - \frac{\lambda}{6k_BT}\right]. \tag{6}$$

λ is the Lagrange multiplier which ensures the normalization condition

$$\sum_{\alpha\beta\gamma\delta}p_{ijkl}^{\alpha\beta\gamma\delta} = 1. \tag{7}$$

For each T and μ_α, an equilibrium state can be obtained by iteration procedure. The tolerance of the probability convergence is 10^{-8} in our calculations.

The ordered and disordered phase of bcc lattice are listed in Table 1. They can be distinguished by the symmetries among the four sites in IT clusters. The order parameters for species α in Table 1 are defined as [46]

$$\begin{aligned}\xi_1(\alpha) &= p_\alpha^i + p_\alpha^j - p_\alpha^k - p_\alpha^l,\\ \xi_2(\alpha) &= p_\alpha^i + p_\alpha^k - p_\alpha^j - p_\alpha^l,\\ \xi_3(\alpha) &= p_\alpha^i + p_\alpha^l - p_\alpha^j - p_\alpha^k.\end{aligned} \tag{8}$$

The A2 phase is disordered one because the four sites are equivalent and the order parameters for n species of the system are zero. While the other three are ordered ones because the symmetry among four sites is broken and the nonzero order parameters appear. Eq. (5) holds

Table 1
Ordered and disordered phases in bcc lattice. The A2 phase is disordered one and the other three are ordered ones.

phase	prototype	point probabilities	order parameters
A2	Fe	$p_\alpha^i = p_\alpha^j = p_\alpha^k = p_\alpha^l$	$\xi_1(\alpha) = \xi_2(\alpha) = \xi_3(\alpha) = 0$
B2	CsCl	$p_\alpha^i = p_\alpha^j \neq p_\alpha^k = p_\alpha^l$	$\xi_1(\alpha) \neq 0, \xi_2(\alpha) = \xi_3(\alpha) = 0$
$D0_3$	BiF_3	$p_\alpha^i \neq p_\alpha^j \neq p_\alpha^k = p_\alpha^l$	$\xi_1(\alpha) \neq 0, \xi_2(\alpha) = \xi_3(\alpha) \neq 0$
B32	NaTl	$p_\alpha^i = p_\alpha^k \neq p_\alpha^j = p_\alpha^l$	$\xi_2(\alpha) \neq 0, \xi_1(\alpha) = \xi_3(\alpha) = 0$

The relations for point probabilities and order parameters hold for every species of the system.

symmetry in iteration procedure [30].

2.3. Cluster expansion method

According to Eq. (2), the formation energy depends on the occupation probabilities $p^{ijkl}_{\alpha\beta\gamma\delta}$. Similarly, a function f of any configuration $\boldsymbol{\sigma}$ can be calculated by CEM [47,48]. For elastic property f, we have

$$f(\sigma) = 6\sum_{\alpha\beta\gamma\delta}\varepsilon(f)_{\alpha\beta\gamma\delta}p^{ijkl}_{\alpha\beta\gamma\delta} + \sum_{\alpha}\nu(f)_{\alpha}x_{\alpha}, \tag{9}$$

where $\nu(f)_{\alpha}$ is the property f for species α, and $\varepsilon(f)_{\alpha\beta\gamma\delta}$ is effective coefficients within the tetrahedron approximation and is expressed by

$$\begin{aligned}\varepsilon(f)_{\alpha\beta\gamma\delta} &= \frac{1}{6}(w(f)^{(1)}_{\alpha\gamma} + w(f)^{(1)}_{\alpha\delta} + w(f)^{(1)}_{\beta\gamma} + w(f)^{(1)}_{\beta\delta}) \\ &\quad + \frac{1}{4}(w(f)^{(2)}_{\alpha\beta} + w(f)^{(2)}_{\gamma\delta}) + \tilde{w}(f)_{\alpha\beta\gamma\delta}.\end{aligned} \tag{10}$$

The coefficients in Eq. (10) are calculated using the methods described in Ref. [37]. Eq. (2) and (3) are the CEM for formation energy U.

3. Results and discussion

3.1. Interaction parameters

The relaxed lattice constants, formation energies, and elastic properties of the phases are listed in Table 2. Since the unit cells of $D0_3$ and B32 structures are $2 \times 2 \times 2$ as the ones of A2 and B2 structures, the lattice constants of A2 and B2 are doubled for easy comparison. The stable phases with notation '†' are the ground states which located on the convex hull lines of energy convex hull where the y-axis is the formation energy and the x-axis is the composition as shown in Fig. 2. The formation energies are used to determine the stable phases and deduce the CVM interaction parameters. The reference states are bcc structures of pure components for simplicity. The reference states are related only to the site energies and do not affect the interaction energies. As the energy difference between antiferromagnetic and nonmagnetic bcc Cr is only 1.3 meV/atom [55], the nonmagnetic Cr reference state is used in our calculations. The energy difference of antiferromagnetic and nonmagnetic bcc Cr only leads to 1% shifting in CVM interaction parameters. The bulk modulus K, shear modulus G and Poisson's ratio ν are obtained by Voight-Reuss-Hill (VRH) approximation [56]. The interaction parameters for phase diagrams and elastic properties calculations are listed in Table 3.

Table 2
Results of first-principles calculations: lattice constants a (Å), formation energies U (eV/atom), bulk moduli K (GPa), shear moduli G (GPa) and Poisson's ratios ν of the system.

compounds	a	U	K	G	ν
Fe-A2†	5.66	0	190.7	79.0	0.318
	5.74[a]	–	173.1[a]	87.5[a]	0.284[a]
	5.68[b]	–	187.0[b]	84.0[b]	0.305[b]
Cr-A2†	5.68	0	261.5	104.4	0.324
	5.76[c]	–	191.0[c]	119.8[c]	0.241[c]
	5.70[d]	–	254.7[d]	128.1[d]	0.285[d]
Al-A2†	6.46	0	61.4	32.6	0.273
	6.44[e]	–	68.8[e]	–	–
FeCr-B2	5.64	0.19	196.4	39.4	0.406
FeCr-B32	5.65	0.09	232.9	35.1	0.428
Fe_3Cr-$D0_3$	5.65	0.06	191.3	88.4	0.230
$FeCr_3$-$D0_3$	5.65	0.12	231.4	102.9	0.306
FeAl-B2†	5.76	− 0.37	175.3	95.4	0.270
	5.82[f]		152.0[f]	–	–
	–	− 0.38[i]	176.0[g]	112.0[g]	0.238[g]
FeAl-B32	5.86	− 0.24	144.1	20.6	0.432
	5.80[h]	− 0.22[i]	169.8[h]	–	–
Fe_3Al-$D0_3$†	5.74	− 0.24	175.1	77.2	0.308
	5.81[g]	− 0.26[i]	152.0[g]	88.0[g]	0.257[g]
$FeAl_3$-$D0_3$	5.99	− 0.08	130.6	59.9	0.301
	5.98[h]	− 0.09[i]	127.4[h]	–	–
CrAl-B2	6.06	− 0.07	128.7	87.3	0.224
	6.10[j]	–	120.2[j]	34.6[j]	0.369[j]
CrAl-B32 ‡	5.89	− 0.12	170.9	78.9	0.300
Cr_3Al-$D0_3$	5.91	− 0.04	210.1	57.9	0.374
$CrAl_3$-$D0_3$	6.12	0.07	81.4	118.0	0.011

[a] Exp. in Ref. [49].
[b] Cal. in Ref. [50].
[c] Exp. in Ref. [51].
[d] Cal. in Ref. [17].
[e] Cal. in Ref. [52].
[f] Exp. in Ref. [53].
[g] Cal. in Ref. [16].
[h] Cal. in Ref. [48].
[i] Cal. in Ref. [54].
[j] Cal. in Ref. [19].

For the phase diagram calculations of Fe-Cr-Al alloy, we only consider bcc and bcc superstructures. The energy convex hulls of Fe-Cr, Fe-Al, and Cr-Al are shown in Fig. 2, and the formation energies for non-bcc stable structures $FeAl_6$-*Cmcm*, Cr_2 Al-I4/mmm, $CrAl_3$-I4/mmm and Cr_7Al_{45}-C2/m from USPEX [57,58] calculations are also included. These non-bcc stable phases are consistent with the phases in Materials Project [59]. In Fig. 2, the stable phases on red solid lines are the stable phases within bcc superstructures, and the ones on black dotted lines are the stable phases beyond bcc superstructures. As we can see, there is no stable intermetallic phase in Fe-Cr alloy, and the non-bcc stable phase $FeAl_6$-*Cmcm* does not affect the stabilities of the bcc ones in Fe-Al alloy. While in Cr-Al alloy, the non-bcc stable phases Cr_2 Al-I4/mmm, $CrAl_3$-I4/mmm and Cr_7Al_{45}-C2/m affect the stability of the bcc one CrAl-B32. The bcc phase CrAl-B32 becomes a metastable phase and notated as '‡' in Table 2.

And also the results computed by others and experimental ones are also listed in Table 2. For the Fe-Cr alloys, there are no experimental results to compare. Our results show linear dependencies of the lattice constant, bulk modulus and shear modulus on concentration, which are in good agreements with the results in Ref. [17]. The lattice constants and bulk moduli of the Fe-Al alloys show good agreement with other experimental and calculated values [16,48–50,52–54]. The slight deviations arise from different calculation methods. As for the Cr-Al alloys, we merely found a B2 phase result by calculation [19].

3.2. Binary phase diagrams

Three binary phase diagrams have been obtained by CVM with the interaction parameters listed in Table 3.

Fig. 3(a) shows the calculated Fe-Cr phase diagram. There is no stable intermetallic phase in the Fe-Cr alloy which is consistent with the result obtained from the first-principles calculations. The maximum critical temperature that separates the solid solution section and miscibility gap is 350 K which is close to the critical temperature 370 K obtained with interaction parameters fitted by experimental data [60]. Experimentally, there was an intermetallic σ phase when temperature is 320 ~ 1103 K [61]. The space group of the σ phase is $P4_2/mnm$ [62], and its possible structures have been investigated by first-principles calculations [63,64]. Since the σ phase is non-bcc lattice, it is not included in the present calculations.

Fig. 3(b) shows the calculated Fe-Al phase diagram. The phase transitions between the A2/B2 and B2/$D0_3$ are the second-order one [40]. The stable intermetallic phases are FeAl-B2 and Fe_3 Al-$D0_3$ which are consistent with the results from first-principles calculations. The main features of the experimental phase diagram are reproduced. The maximum critical temperatures for the A2/B2 and B2/$D0_3$ transition are 3200 K and 1015 K respectively, which are consistent with pervious calculations [40]. The low solubility of Fe in Al-A2 is in good agreement with the experimental results [65]. And the large phase separation in Al-rich region corresponds to three non-bcc experimental intermetallic phases $FeAl_2$, Fe_2Al_5, and $FeAl_3$, as well as the phase separations

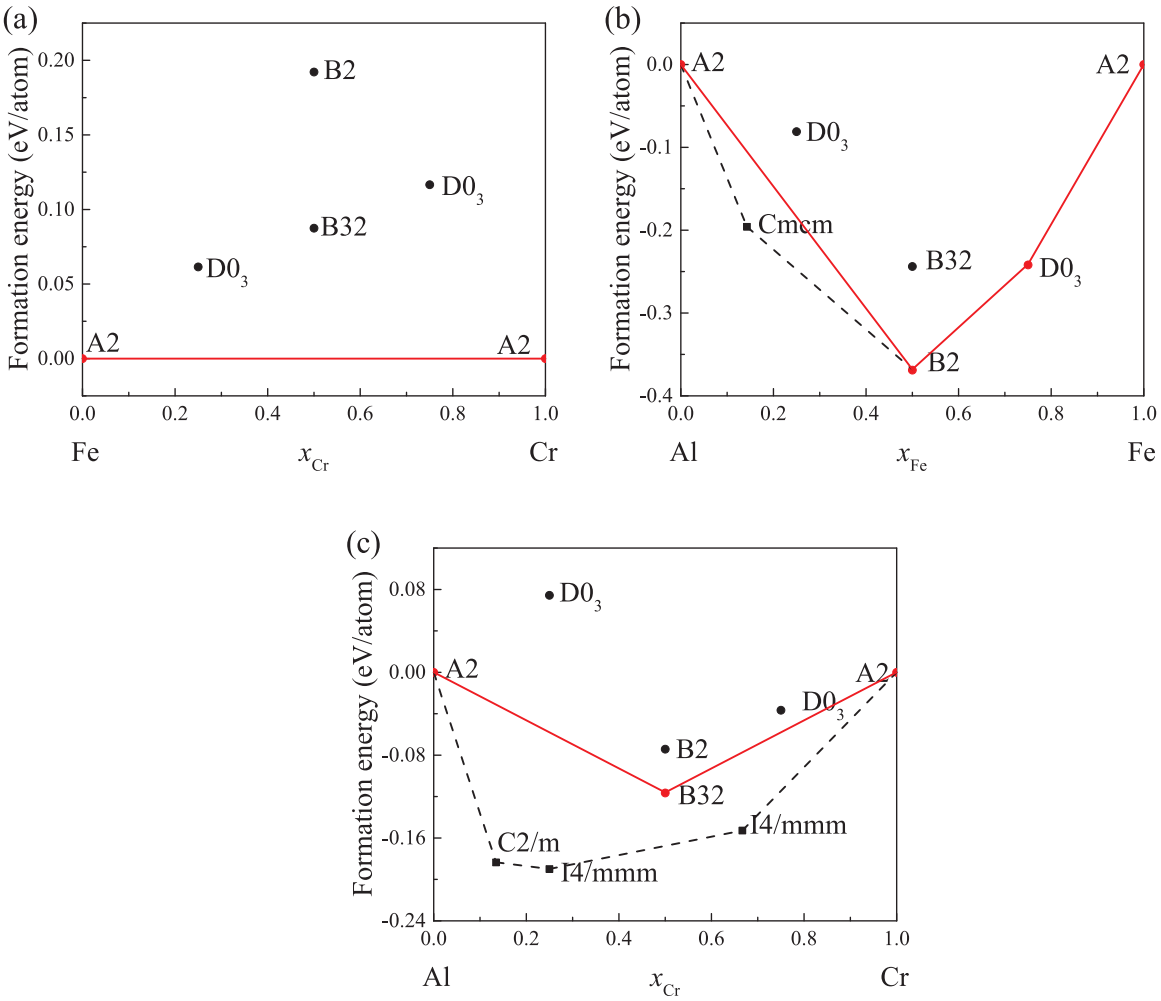

Fig. 2. (a)-(c) Energy convex hulls of Fe-Cr, Fe-Al, and Cr-Al alloys. Red solid and black dotted lines correspond to the convex hull lines within and beyond bcc superlattices. (For interpretation of the references to color in this figure legend, the reader is referred to the web version of this article).

Table 3
Interaction parameters for phase diagrams and elastic properties calculations. Phase diagrams: formation energies $U(10^{-2}$ eV/atom). Elastic properties: bulk moduli K(GPa), shear moduli G(GPa), and Poisson's ratios $\nu(10^{-2})$.

α	β	f	$w(f)^{(1)}_{\alpha\beta}$	$w(f)^{(2)}_{\alpha\beta}$	$\bar{w}(f)_{\alpha\beta\alpha\beta}$	$\bar{w}(f)_{\alpha\beta\beta\beta}$
Fe	Cr	U	4.80	− 2.31	1.01	0.92
		K	− 7.42	− 1.53	4.38	0.80
		G	− 13.08	19.44	− 14.80	0.31
		ν	2.13	− 4.14	3.15	0.06
Fe	Al	U	− 1.86	0.04	− 1.34	1.85
		K	12.31	− 5.27	1.54	3.36
		G	9.89	− 6.68	− 5.83	0.99
		ν	− 0.66	0.93	2.01	0.25
Cr	Al	U	− 9.22	− 3.83	0.93	2.68
		K	− 8.18	10.02	− 0.71	− 4.78
		G	4.68	− 25.30	12.82	16.01
		ν	− 1.89	6.68	− 2.70	− 5.63

between them [65]. We notice that the experimental critical temperature of A2/B2 transition is 1750 K [66]. Since the maximum temperature of B2 phase in experiment is the peritectic temperature, which leads to liquid phase cap on the temperature scale, we can not compare our maximum critical temperature with the experimental one. Also we ignore the phonon effect which can lead to a reduction of ~ 10% in temperature scale [38].

In Fig. 3(c), we show the calculated Cr-Al phase diagram. There is only one metastable intermetallic phase CrAl-B32 as shown in Table 2. The maximum transition temperature for the A2/B32 transition is 1395 K at 48 at% Al. The only ordered compound B32 shows a narrow stability range near the equiatomic composition. The nonzero Al solubility in Cr begins at 300 K and the solubility increases to 30 at% Al at 900 K. The phase separation A2(Cr) + B32 in the Cr-rich region is in good agreement with the experimental results [67]. The other phase separation A2(Al) + B32 in the Al-rich region corresponds to the non-bcc phases determined by the experimental methods [67,68]. The Cr-Al phase diagram obtained by Eleno using CVM method shows two stable ordered phases B2 and $D0_3$ [39], and the B2 and $D0_3$ ordering phenomena are due to the interaction parameters derived from the experimental data at the temperature where B2 phase exists [67].

3.3. Ternary isothermal phase diagrams

Fig. 4 shows the isothermal sections of the Fe-Cr-Al phase diagrams from 600 to 3000 K. Since the only stable phase in the Fe-Cr alloys is solid solution, all these isothermal phase diagrams give the disordered phase along the FeCr axis. The ordered phases in the Fe-Al and Cr-Al alloys are dissolved with the third component, resulting in an extension of binary ordered phases to the ternary region.

The isothermal section at 600 K shows more complex phases than other sections. There is a wide phase separation at the Al-rich corner. The solubility of Fe in the Cr-Al binary phase is small and thus there is only a small sector for the ternary extension of CrAl-B32 and a narrow

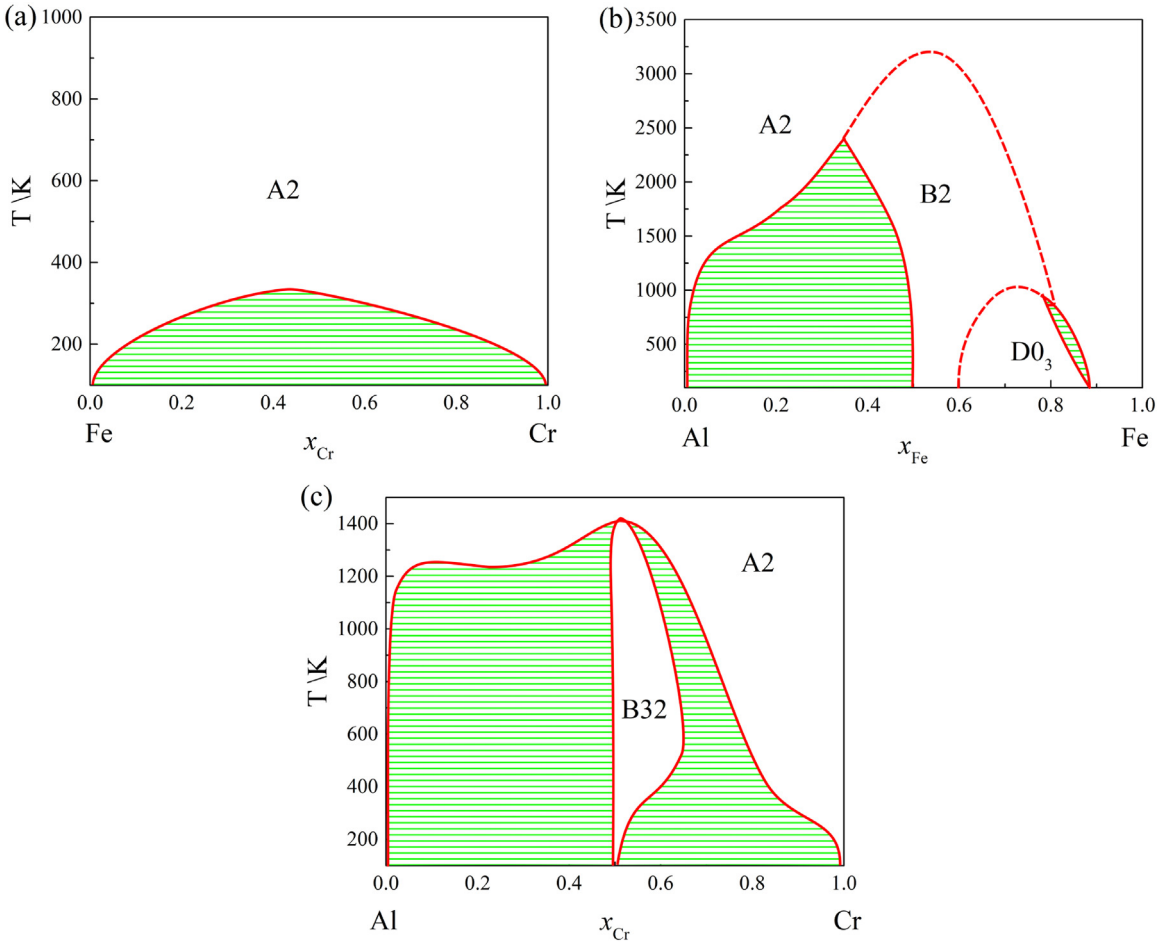

Fig. 3. (a)-(c) Phase diagrams of Fe-Cr, Fe-Al, and Cr-Al systems. Red solid and dotted lines correspond to the first- and second-order phase transitions, respectively. The shaded areas are the phase separation regions. (For interpretation of the references to color in this figure legend, the reader is referred to the web version of this article).

extension of Cr-A2. While the solubility of Cr in the Fe-Al alloys approaches 90 at%Cr, resulting in three triangle regions for the extended binary phases B2, $D0_3$, and A2. Furthermore, a ternary ordered phase B32 appears which is located between the ternary extension of FeAl-B2 and the phase separation A2(Cr) + B32(CrAl). It may be considered as a transitional phase between two extensions of equiatomic binary phases FeAl-B2 and CrAl-B32.

The ternary ordered phase B32 gives two sets of equivalence sites i, k and j, l see Table 1, and the occupation probabilities show different behavior from the binary extension phases where the third component have equal occupation probabilities at four sites i, j, k, l. Near the phase separation boundary, the i, k sites are mainly occupied by the Cr, Al atoms ($p^i_{Cr} > p^i_{Al} \gg p^i_{Fe}$), and the j, l sites are mainly occupied by Cr atoms, while Fe and Al atoms have the same occupied probabilities ($p^j_{Cr} > p^j_{Al} = p^j_{Fe}$). Near the FeAl-B2 phase, the occupation probabilities of Fe on the i and k sites increase and those of Al on the i and k sites decrease, resulting in a tendency of reducing the difference between the two sets of sites. The A2 like occupation probabilities of Fe and Al atoms appear at the phase boundary B32/FeAl-B2, causing the extension FeAl-B2 phase.

As temperature increases, the compositional intervals of the disordered phases in the binary alloys become wider and the solubility of the third component increases as well, resulting in the extension of the disordered phases. Meanwhile the compositional intervals of the ordered phases in the binary alloys become smaller and the solubility of the third component decreases, resulting in the reduction of extensions of the ordered phases. As temperature reaches 800 K, the only ternary ordered phase B32 disappears. The significant reduction occurs in the extensions of Cr-Al ordered phases. There is a slight increase of Al solubility in the ternary extensions of Fe-Al binary phases B2, $D0_3$, and A2. At 1000 K, the ternary extension of FeAl-$D0_3$ disappear. The ternary extensions of Cr-Al ordered phases also disappear and is replaced by a solid solution A2 phase.

As temperature increases to 2000 K, the main feature of the section is that there are wide A2 phases and the ternary extension of FeAl-B2, and the phase separation between them remains. When temperature increases to 3000 K, the phase separation is deflated to a second-order phase transition, and the solubility of Cr in the extended FeAl-B2 ternary phase is 18 at%. The ternary extension of the FeAl-B2 phase disappears when temperature above 3200 K. The effect of phonon which is not considered in our rigid lattice CVM model gets more important with the temperature up to 2000 K. Kikuchi comes up with a continuous displacement model which is beyond rigid lattice assumption by introducing the atom degrees of freedom [40], and Mohri and Chen handle the vibrational degrees of freedom by using a Deybe-Grünneisen model [38]. Both of them get a reduction of temperature in phase diagrams.

3.4. Elastic properties

Elastic properties of Fe-Cr-Al alloys have been obtained by CEM with the interaction parameters listed in Table 3. We focus on bulk modulus K, shear modulus G and Poisson's ratio ν.

Fig. 5 shows the calculated bulk moduli K at 600 K ~ 3000 K using

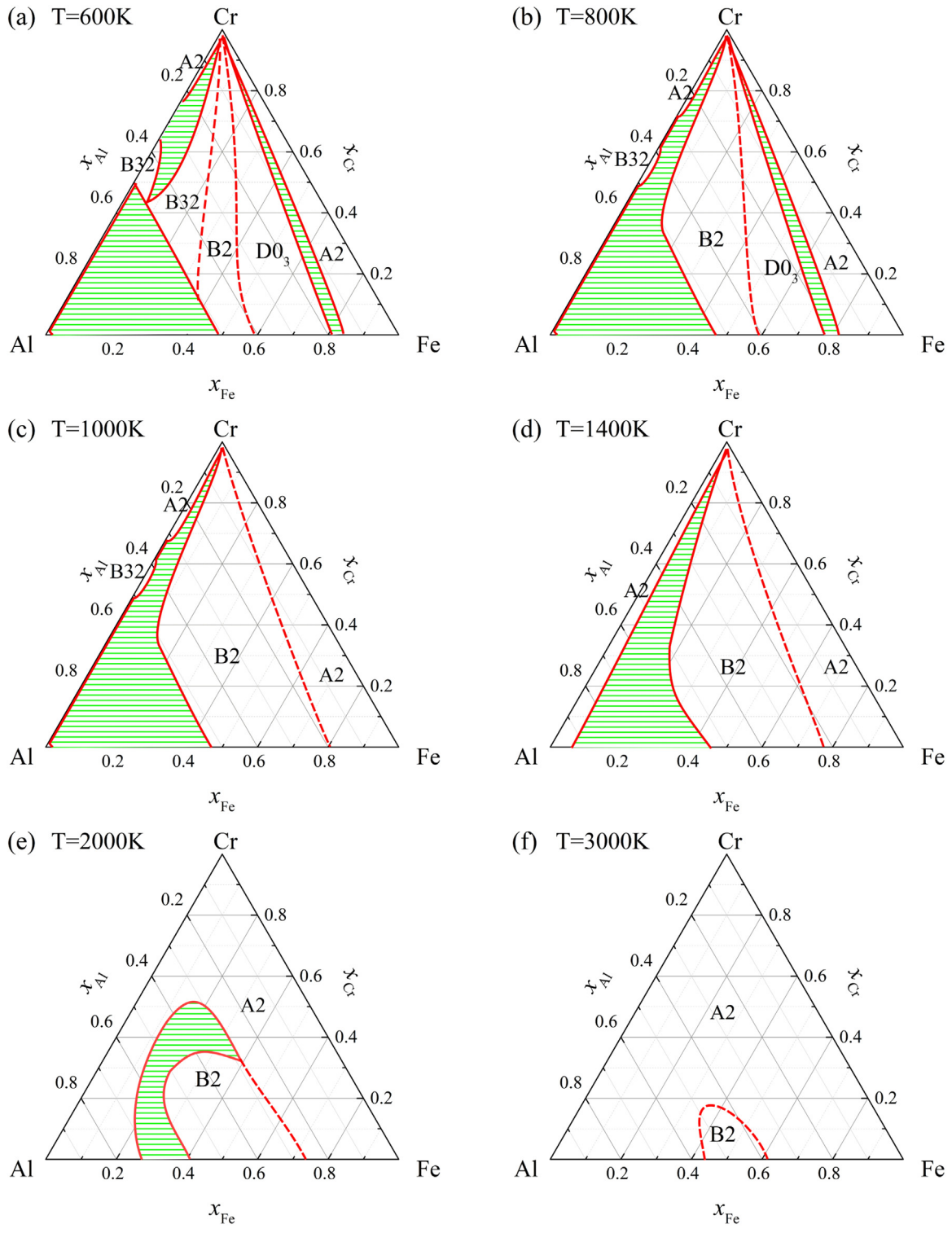

Fig. 4. (a)-(f) Ternary isothermal phase diagrams of Fe-Cr-Al system at 600 K ~ 3000 K. Red solid and dotted lines correspond to the first- and second-order phase transitions, respectively. The shaded areas are the phase separation regions. (For interpretation of the references to color in this figure legend, the reader is referred to the web version of this article).

CEM method. There is a significant reduction in bulk modulus with increasing Al concentration at the FeAl and CrAl axes, which is consistent with the tendency shown in Ref. [16,15]. While a modest reduction with increasing Fe at the FeCr axis presents the same trend as previous first-principles calculations [17,18]. The maximum of bulk modulus K is located at Cr-rich corner and the minimum is located at $x_{Al} = 0.5at\%$ ($T < 1400$ K) or Al-rich corner ($T > 1400$ K). The bulk modulus shows a nearly linear concentration dependency among all compositional ranges. As temperature increases, a slight reduction in bulk modulus is presented, which is consistent with the results in Ref. [19,20]. The ordering dependence of bulk modulus is weak at all temperatures.

Fig. 6 shows the calculated shear moduli G at 600 ~ 3000 K. The significant reduction in shear modulus with increasing Fe concentration

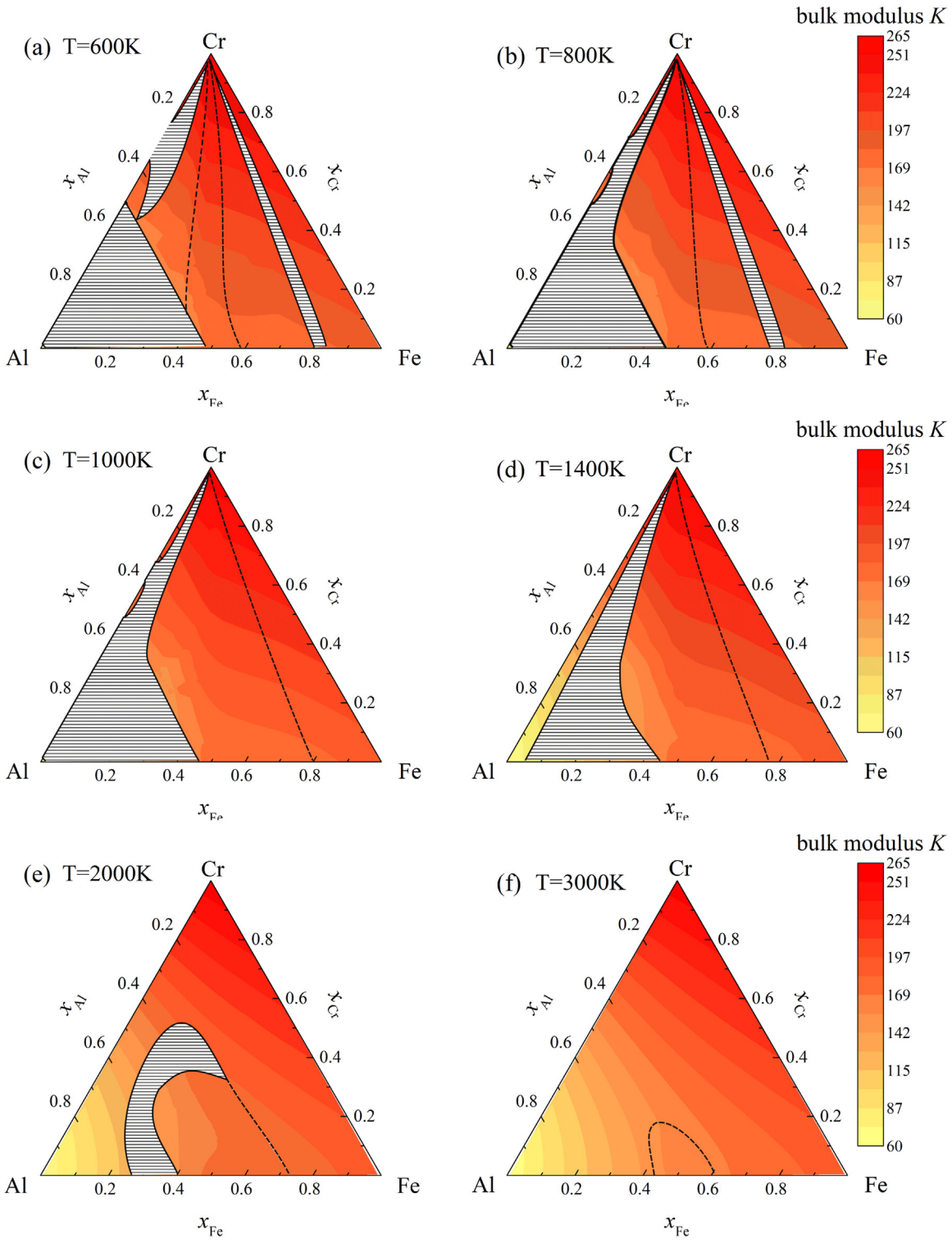

Fig. 5. (a)-(f) The bulk moduli K at 600 K ~ 3000 K. Solid and dotted lines correspond to the first- and second-order phase transitions, respectively. The shaded areas are the phase separation regions.

at the FeCr axis presents the same trend as previous calculation [17]. And also a reduction with increasing temperature is observed, which is in consistent with the previous calculations [19]. The exception of increasing in shear modulus happened at 2000–3000 K. Above 2000 K, the alloys become liquid [69,22]. In our calculations, the liquid effect is ignored. We can see that the maximum of shear modulus is located at the ternary extension of FeAl-B2 below 1400 K, and it relates to the large solubility of Cr in Fe-Al alloys and the arise of ordered FeAl-B2 extension phase. In comparing with the results of bulk modulus in Fig. 5, the shear modulus is sensitive to ordering and temperature.

Fig. 7 shows the calculated Poisson's ratio ν at 600 ~ 3000 K. Our result shows that the Poisson's ratio has the value between 0.2 and 0.35 in Figs. 7(a)-(e). Since when $T > 2000$ K the system is a liquid [22,69] and the liquid effect is ignored in our calculation, we focus on the cases where $T < 2000$ K. The Poisson's ratio ν is almost linear along the FeCr axis, which is in a good agreement with the previously calculated

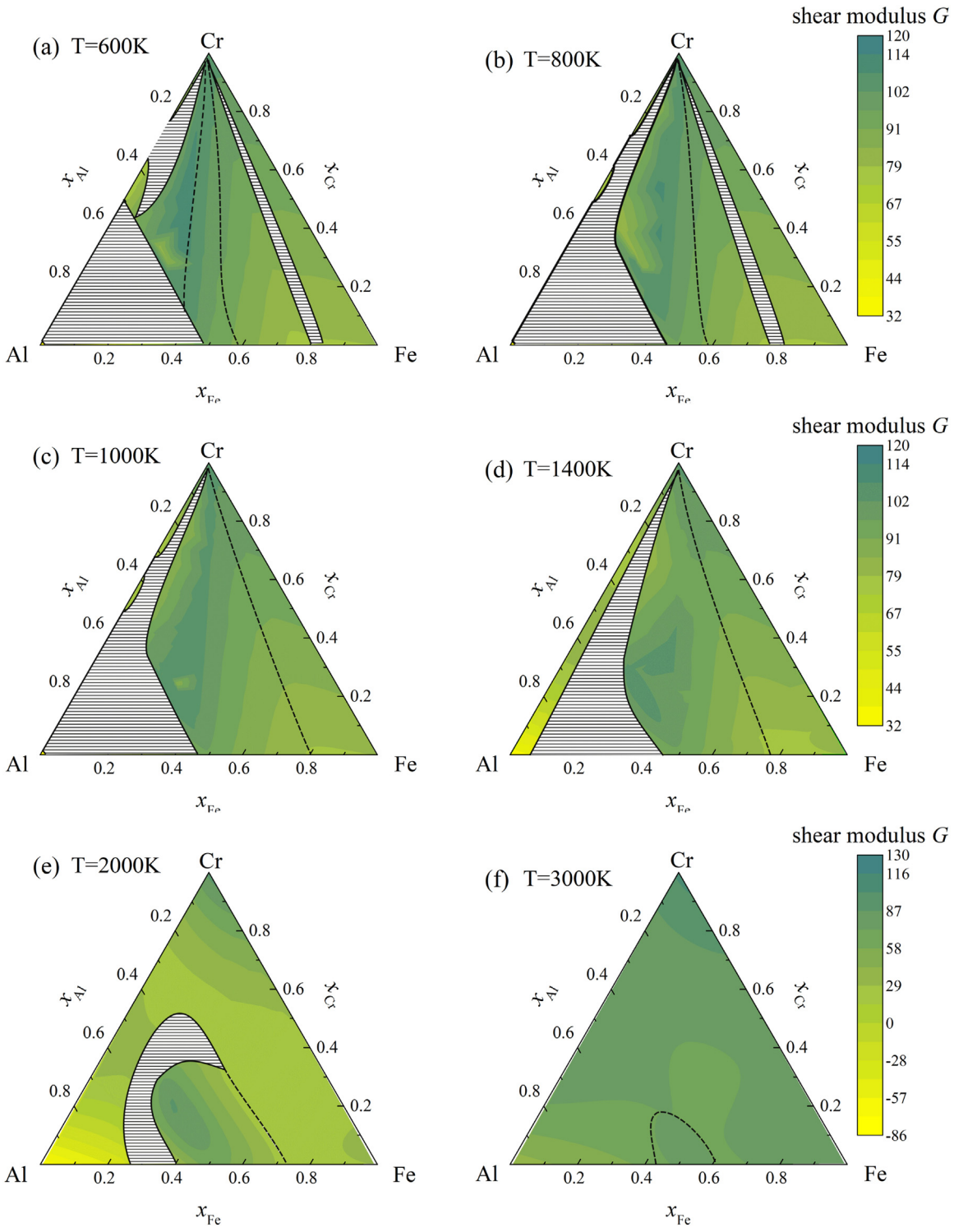

Fig. 6. (a)-(f) The shear moduli G at 600 K ~ 3000 K. Solid and dotted lines correspond to the first- and second-order phase transitions, respectively. The shaded areas are the phase separation regions.

results [17]. In Table 2, we can see that the phases with low Poisson's ratios are $CrAl_3 - D0_3$, CrAl-B2 and Al-A2, indicating that the solution of Al can reduce the Poisson's ratio. As the Al rich region are mainly phase separation at $T < 2000$ K, a minimum of Poisson's ratio is located near the 50 at% Al. Comparing with Fig. 4 and 7, the ordered phase has more lower Poisson's ratio than disordered one. Also the temperature dependence of Poisson's ratio is weak.

The blue lines in Fig. 7 correspond to brittle-ductile critical value $\nu = 0.26$ of Pugh's criteria [70]. The materials with the value $\nu > 0.26$ ($\nu < 0.26$) have ductile (brittle) character. Disordered Fe-Cr alloys with a little Al solvent keeps the ductile property, while Al-rich corner and ternary extended FeAl-B2 ordered phases exhibit brittle property, in agreement with experimental observation [71]. It can be seen that concentration dependency near FeCr axis is modest, and the addition of Al can soften both bulk modulus and Poisson's ratio. The different influence between Al solvent and Fe, Cr solvent in Fe-Cr-Al alloys origins from the mismatch in lattice constants of them at zero temperature listed in Table 2. The concentration dependency, as well as the

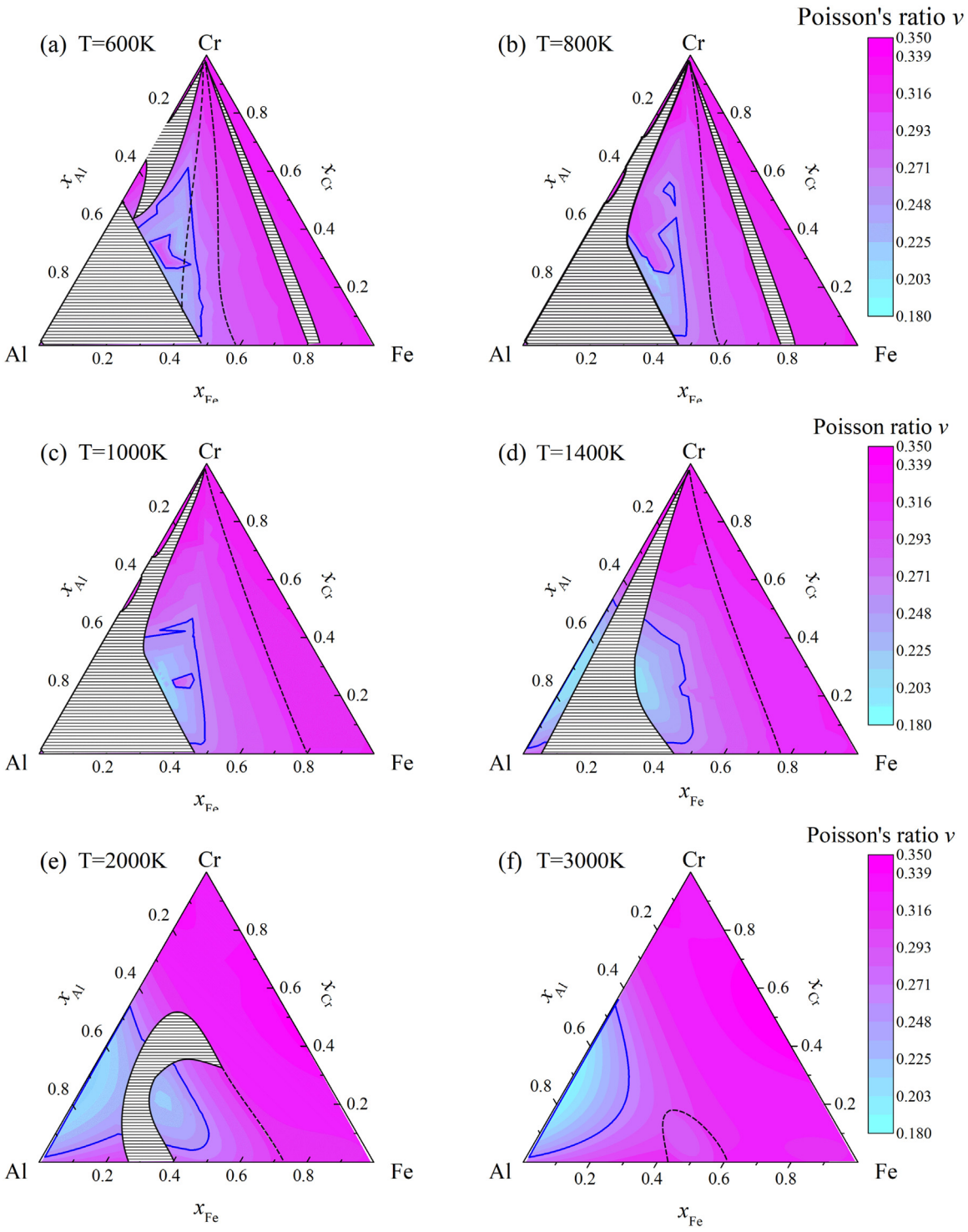

Fig. 7. (a)-(f) The Poisson's ratio v at 600 ~ 3000 K. Solid and dotted lines correspond to the first- and second-order phase transitions, respectively. The shaded areas are the phase separation regions. The blue lines correspond to brittle-ductile critical value $v = 0.26$ of Pugh's criteria.

temperature and ordering dependencies is presented. Bulk modulus K and Poisson's ratio v show weak ordering and temperature dependencies, while shear modulus G shows a significant reduction with increase of temperature, and the ordering also improves the resistance of shear deformation.

4. Conclusions

In summary, we have investigated the phase diagrams and elastic properties of Fe-Cr-Al alloys in full-temperature and all-compositional ranges based on first-principles calculations combined with CVM and CEM method.

For phase diagrams, our calculations are consistent with results obtained by experimental and other theoretical methods. We find that a new ternary phase B32 appears in 600 K isothermal phase diagram. The B32 symmetry holds for all three components. The solubility difference is observed in ternary phase diagrams, the binary FeAl phases show an extremely high solubility for Cr, while the binary CrAl phase has a low

solubility for Fe.

For elastic properties bulk modulus, shear modulus and Poisson's ratio, our results reveal the changes tendency among temperature, ordering and concentration. The concentration dependency near FeCr axis is modest, and the addition of Al softens both bulk modulus and Poisson's ratio. Bulk modulus K and Poisson's ratio ν show weak ordering and temperature dependencies. Shear modulus G exhibits a significant reduction with the increase of temperature, and the ordering improve the resistance of shear deformation. The isothermal Poisson's ratio results show that disordered Fe-Cr alloys with Al solvent exhibit ductile property, while the Al-rich corner displays brittle property.

Acknowledgements

This research was supported by the National Key Research and Development Program of China [Grant No. 2016YFB0700102].

Data availability statement

The raw/processed data required to reproduce these findings cannot be shared at this time as the data also forms part of an ongoing study.

References

[1] M. Palm, Concepts derived from phase diagram studies for the strengthening of Fe-Al-based alloys, Intermetallics 13 (2005) 1286–1295, https://doi.org/10.1016/j.intermet.2004.10.015.
[2] A. Velon, D.-Q. Yi, Influence of Cr on the oxidation of Fe_3Al and Ni_3Al at 500 °C, Oxid. Met. 57 (2002) 13–31, https://doi.org/10.1023/A:1013386427567.
[3] C. Badini, F. Laurella, Oxidation of FeCrAl alloy: influence of temperature and atmosphere on scale growth rate and mechanism, Surf. Coat. Technol. 135 (2001) 291–298, https://doi.org/10.1016/S0257-8972(00)00989-0.
[4] E. Airiskallio, E. Nurmi, M. Heinonen, I. Väyrynen, K. Kokko, M. Ropo, M. Punkkinen, H. Pitkänen, M. Alatalo, J. Kollár, B. Johansson, L. Vitos, High temperature oxidation of Fe-Al and Fe-Cr-Al alloys: the role of Cr as a chemically active element, Corros. Sci. 52 (2010) 3394–3404, https://doi.org/10.1016/j.corsci.2010.06.019.
[5] R. Cueff, H. Buscail, E. Caudron, F. Riffard, C. Issartel, S.E. Messki, Effect of reactive element oxide coating on the high temperature oxidation behaviour of FeCrAl alloys, Appl. Surf. Sci. 229 (2004) 233–241, https://doi.org/10.1016/j.apsusc.2004.01.072.
[6] K. Terrani, S. Zinkle, L. Snead, Advanced oxidation-resistant iron-based alloys for LWR fuel cladding, J. Nucl. Mater. 448 (2014) 420–435, https://doi.org/10.1016/j.jnucmat.2013.06.041.
[7] J.K. Bunn, R.L. Fang, M.R. Albing, A. Mehta, M.J. Kramer, M.F. Besser, J.R. Hattrick-Simpers, A high-throughput investigation of Fe-Cr-Al as a novel high-temperature coating for nuclear cladding materials, Nanotechnology 26 (2015) 274003.
[8] J. Ejenstam, M. Thuvander, P. Olsson, F. Rave, P. Szakalos, Microstructural stability of Fe-Cr-Al alloys at 450 − 550 °C, J. Nucl. Mater. 457 (2015) 291–297, https://doi.org/10.1016/j.jnucmat.2014.11.101.
[9] K.G. Field, S.A. Briggs, K. Sridharan, R.H. Howard, Y. Yamamoto, Mechanical properties of neutron-irradiated model and commercial FeCrAl alloys, J. Nucl. Mater. 489 (2017) 118–128, https://doi.org/10.1016/j.jnucmat.2017.03.038.
[10] S. Kobayashi, T. Takasugi, Mapping of 475 °C embrittlement in ferritic Fe-Cr-Al alloys, Scr. Mater. 63 (2010) 1104–1107, https://doi.org/10.1016/j.scriptamat.2010.08.015.
[11] K.G. Field, X. Hu, K.C. Littrell, Y. Yamamoto, L.L. Snead, Radiation tolerance of neutron-irradiated model Fe-Cr-Al alloys, J. Nucl. Mater. 465 (2015) 746–755, https://doi.org/10.1016/j.jnucmat.2015.06.023.
[12] E.A. Campo, Mechanical properties of polymeric materials, in: E.A. Campo (Ed.), Selection of Polymeric Materials, Plastics Design Library, William Andrew Publishing, Norwich, NY, 2008.
[13] G.N. Greaves, A.L. Greer, R.S. Lakes, T. Rouxel, Poisson's ratio and modern materials, Nat. Mater. 10 (2011) 823, https://doi.org/10.1038/nmat3134.
[14] D. Rosato, D. Rosato, Design parameter, in: D. Rosato, D. Rosato (Eds.), Plastics Engineered Product Design, Elsevier Science, Amsterdam, 2003, pp. 161–197.
[15] Y. Liu, X. Chong, Y. Jiang, R. Zhou, J. Feng, Mechanical properties and electronic structures of Fe-Al intermetallic, Phys. B Condens. Matter 506 (2017) 1–11, https://doi.org/10.1016/j.physb.2016.10.032.
[16] S.J. Kang, S. Park, M. Kim, H.N. Han, S.-K. Lee, K.Y. Lee, Y.-K. Kwon, Enhanced mechanical property of Fe-Al alloy due to Mn insertion: ab initio study, J. Alloy. Compd. 583 (2014) 295–299, https://doi.org/10.1016/j.jallcom.2013.08.167.
[17] V.I. Razumovskiy, A.V. Ruban, P.A. Korzhavyi, First-principles study of elastic properties of Cr- and Fe-rich Fe-Cr alloys, Phys. Rev. B 84 (2011) 024106, https://doi.org/10.1103/PhysRevB.84.024106.
[18] H. Zhang, B. Johansson, L. Vitos, Ab initio calculations of elastic properties of bcc Fe-Mg and Fe-Cr random alloys, Phys. Rev. B 79 (2009) 224201, https://doi.org/10.1103/PhysRevB.79.224201.
[19] H. Faraoun, H. Aourag, C. Esling, J. Seichepine, C. Coddet, Elastic properties of binary NiAl, NiCr and AlCr and ternary Ni_2AlCr alloys from molecular dynamic and abinitio simulation, Comput. Mater. Sci. 33 (2005) 184–191, https://doi.org/10.1016/j.commatsci.2004.12.011.
[20] L.-F. Zhu, M. Friák, A. Udyansky, D. Ma, A. Schlieter, U. Kühn, J. Eckert, J. Neugebauer, Ab initio based study of finite-temperature structural, elastic and thermodynamic properties of FeTi, Intermetallics 45 (2014) 11–17, https://doi.org/10.1016/j.intermet.2013.09.008.
[21] G.V. Raynor, V.G. Rivlin, Phase equilibria in iron ternary alloys-a critical assessment of the experimental literature, Inst. Met. (1988) 81–97.
[22] V. Raghavan, Al-Cr-Fe (Aluminum-Chromium-Iron), J. Phase Equilib. Diff 33 (2012) 55–58, https://doi.org/10.1007/s11669-012-9981-7.
[23] M. Palm, The Al-Cr-Fe system phases and phase equilibria in the Al-rich corner, J. Alloy. Compd. 252 (1997) 192–200, https://doi.org/10.1016/S0925-8388(96)02719-3.
[24] D. Pavlyuchkov, S. Balanetskyy, W. Kowalski, M. Surowiec, B. Grushko, Stable decagonal quasicrystals in the Al-Fe-Cr and Al-Fe-Mn alloy systems, J. Alloy. Compd. 477 (2009) L41–L44, https://doi.org/10.1016/j.jallcom.2008.11.005.
[25] D.V. Pavlyuchkov, B. Przepiorzynski, B. Grushko, T.Y. Velikanova, Complex orthorhombic phase in the Al-Cr-Fe system, Powder Metall. Met. Ceram. 47 (2008) 698–701, https://doi.org/10.1007/s11106-009-9081-3.
[26] V.G. Khoruzha, K.E. Kornienko, D.V. Pavlyuchkov, B. Grushko, T.Y. Velikanova, The Al-Cr-Fe phase diagram. i. Phase equilibria at subsolidus temperatures over composition range 58-100 at% Al, Powder Metall. Met. Ceram. 50 (2011) 83–97, https://doi.org/10.1007/s11106-011-9306-0.
[27] D. Pavlyuchkov, B. Przepiórzyński, W. Kowalski, T. Velikanova, B. Grushko, Al-Cr-Fe phase diagram. isothermal sections in the region above 50 at% Al, Calphad 45 (2014) 194–203, https://doi.org/10.1016/j.calphad.2013.12.007.
[28] N. Saunders, V. Rivlin, A critical-review and thermodynamic calculations for the Al-rich portion of the Al-Cr-Fe phase-diagram, Z. Metallkd. 78 (1987) 795–801.
[29] M. Jacobs, R. Schmid-Fetzer, T. Markus, V. Motalov, G. Borchardt, K.-H. Spitzer, Thermodynamics and diffusion in ternary Fe-Al-Cr alloys, Part I: thermodynamic modeling, Intermetallics 16 (2008) 995–1005, https://doi.org/10.1016/j.intermet.2008.04.020.
[30] R. Kikuchi, A theory of cooperative phenomena, Phys. Rev. 81 (1951) 988–1003, https://doi.org/10.1103/PhysRev.81.988.
[31] R. Kikuchi, Superposition approximation and natural iteration calculation in cluster variation method, J. Chem. Phys. 60 (1974) 1071–1080, https://doi.org/10.1063/1.1681115.
[32] J.W.D. Connolly, A.R. Williams, Density-functional theory applied to phase transformations in transition-metal alloys, Phys. Rev. B 27 (1983) 5169–5172, https://doi.org/10.1103/PhysRevB.27.5169.
[33] G. Kresse, J. Furthmüller, Efficiency of ab-initio total energy calculations for metals and semiconductors using a plane-wave basis set, Comput. Mater. Sci. 6 (1996) 15–50, https://doi.org/10.1016/0927-0256(96)00008-0.
[34] G. Kresse, J. Furthmüller, Efficient iterative schemes for ab initio total-energy calculations using a plane-wave basis set, Phys. Rev. B 54 (1996) 11169–11186, https://doi.org/10.1103/PhysRevB.54.11169.
[35] P.E. Blöchl, Projector augmented-wave method, Phys. Rev. B 50 (1994) 17953–17979, https://doi.org/10.1103/PhysRevB.50.17953.
[36] J.P. Perdew, K. Burke, M. Ernzerhof, Generalized gradient approximation made simple, Phys. Rev. Lett. 77 (1996) 3865–3868, https://doi.org/10.1103/PhysRevLett.77.3865.
[37] L. Shi, J. Ni, Kinetic-anisotropy-induced ordering-orientation transition in epitaxial growth: a method to synthesize ordering-orientation superlattices, Phys. Rev. Lett. 97 (2006) 126105, https://doi.org/10.1103/PhysRevLett.97.126105.
[38] T. Mohri, Y. Chen, First-principles investigation of $L1_0$-disorder phase equilibria of Fe-Ni, -Pd, and -Pt binary alloy systems, J. Alloy. Compd. 383 (1) (2004) 23–31, https://doi.org/10.1016/j.jallcom.2004.04.030.
[39] L.T.F. Eleno, C.G. Schön, CVM calculation of the b.c.c. Co-Cr-Al phase diagram, Calphad 27 (2003) 335–342, https://doi.org/10.1016/j.calphad.2003.11.003.
[40] P.G. Gonzales-Ormeño, H.M. Petrilli, C.G. Schön, Ab initio calculation of the bcc Fe-Al phase diagram including magnetic interactions, Scr. Mater. 54 (2006) 1271–1276, https://doi.org/10.1016/j.scriptamat.2005.12.024.
[41] H. Ackermann, G. Inden, R. Kikuchi, Tetrahedron approximation of the cluster variation method for b.c.c. alloys, Acta Metall. 37 (1989) 1–7, https://doi.org/10.1016/0001-6160(89)90259-9.
[42] J. Ni, S. Iwata, Phase diagrams of the Blume-Emery-Griffiths model for semiconducting alloy systems $(ABD_2)_{1-x}(CD)_{2x}$ or $[(AB)_{1-x}C_{2x}]D_2$, Phys. Rev. B 52 (1995) 3214–3219, https://doi.org/10.1103/PhysRevB.52.3214.
[43] C.G. Schön, G. Inden, L.T.F. Eleno, Comparison between monte carlo and cluster variation method calculations in the bcc Fe-Al system including tetrahedron interactions, Z. Metallkd. 95 (2004) 459–463, https://doi.org/10.3139/146.017979.
[44] I. Ohnuma, C. Schön, R. Kainuma, G. Inden, K. Ishida, Ordering and phase separation in the b.c.c. phase of the Fe-Al-Ti system, Acta Mater. 46 (1998) 2083–2094, https://doi.org/10.1016/S1359-6454(97)00376-5.
[45] R. Kikuchi, C. van Baal, Phase diagrams of FCC and BCC ordered alloys, Scr. Metall. 8 (1974) 425–429, https://doi.org/10.1016/0036-9748(74)90148-3.
[46] D.A. Contreras-Solorio, F. Mejía-Lira, J.L. Morán-López, J.M. Sanchez, Modeling of the Fe-Al phase diagram, Phys. Rev. B 38 (1988) 11481–11485, https://doi.org/10.1103/PhysRevB.38.11481.
[47] N.A. Zarkevich, D.D. Johnson, Reliable first-principles alloy thermodynamics via truncated cluster expansions, Phys. Rev. Lett. 92 (2004) 255702, https://doi.org/10.1103/PhysRevLett.92.255702.
[48] F. Lechermann, M. Fähnle, J. Sanchez, First-principles investigation of the Ni-Fe-Al

system, Intermetallics 13 (2005) 1096–1109, https://doi.org/10.1016/j.intermet.2005.02.009.
[49] J.A. Rayne, B.S. Chandrasekhar, Elastic constants of iron from 4.2 to 300° K, Phys. Rev. 122 (1961) 1714–1716, https://doi.org/10.1103/PhysRev.122.1714.
[50] K.J. Caspersen, A. Lew, M. Ortiz, E.A. Carter, Importance of shear in the bcc-to-hcp transformation in iron, Phys. Rev. Lett. 93 (2004) 115501, https://doi.org/10.1103/PhysRevLett.93.115501.
[51] M.M. Schwickert, G.Y. Guo, M.A. Tomaz, W.L. O'Brien, G.R. Harp, X-ray magnetic linear dichroism in absorption at the *l* edge of metallic Co, Fe, Cr, and V, Phys. Rev. B 58 (1998) R4289–R4292, https://doi.org/10.1103/PhysRevB.58.R4289.
[52] J.C. Boettger, S.B. Trickey, High-precision calculation of the equation of state and crystallographic phase stability for aluminum, Phys. Rev. B 53 (1996) 3007–3012, https://doi.org/10.1103/PhysRevB.53.3007.
[53] C. Fu, M. Yoo, Deformation behavior of B2 type aluminides: feal and NiAl, Acta Metall. Mater. 40 (1992) 703–711, https://doi.org/10.1016/0956-7151(92)90012-4.
[54] P.G. Gonzales-Ormeño, H.M. Petrilli, C.G. Schön, Ab-initio calculations of the formation energies of bcc-based superlattices in the Fe-Al system, Calphad 26 (2002) 573–582, https://doi.org/10.1016/S0364-5916(02)80009-8.
[55] R. Hafner, D. Spišák, R. Lorenz, J. Hafner, Magnetic ground state of Cr in density-functional theory, Phys. Rev. B 65 (2002) 184432, https://doi.org/10.1103/PhysRevB.65.184432.
[56] R. Hill, The elastic behaviour of a crystalline aggregate, Proc. Phys. Soc. A 65 (1952) 349.
[57] A.R. Oganov, C.W. Glass, Crystal structure prediction using ab initio evolutionary techniques: principles and applications, J. Chem. Phys. 124 (2006) 244704, https://doi.org/10.1063/1.2210932.
[58] A.O. Lyakhov, A.R. Oganov, H.T. Stokes, Q. Zhu, New developments in evolutionary structure prediction algorithm USPEX, Comp. Phys. Comm. 184 (2013) 1172–1182.
[59] S.P. Ong, L. Wang, B. Kang, G. Ceder, Li-Fe-P-O_2 phase diagram from first principles calculations, Chem. Mater. 20 (2008) 1798–1807.
[60] G. Inden, C.G. Schön, Thermodynamic self-consistency issues related to the cluster variation method: the case of the BCC Cr-Fe (Chromium-Iron) system, Calphad 32 (2008) 661–668, https://doi.org/10.1016/j.calphad.2008.09.012.
[61] H. Okamoto, H. Baker (Ed.), ASM Handbook: Volume 3: Alloy Phase Diagrams, ASM International, Materials Park, OH, 1992.
[62] J.M. Joubert, Crystal chemistry and calphad modeling of the σ phase, Prog. Mater. Sci. 53 (2008) 528–583, https://doi.org/10.1016/j.pmatsci.2007.04.001.
[63] M.H.F. Sluiter, K. Esfarjani, Y. Kawazoe, Site occupation reversal in the Fe-Cr σ phase, Phys. Rev. Lett. 75 (1995) 3142–3145, https://doi.org/10.1103/PhysRevLett.75.3142.
[64] J. Havránková, J. Vřeštál, L.G. Wang, M. Šob, Ab initio analysis of energetics of σ-phase formation in Cr-based systems, Phys. Rev. B 63 (2001) 174104, https://doi.org/10.1103/PhysRevB.63.174104.
[65] U. Kattner, B. Burton, H. Okamoto (Ed.), Phase Diagrams of Binary Iron Alloys, ASM international, Materials Park, OH, 1993.
[66] C. Schön, G. Inden, Concentration dependence of the excess specific heat capacity and of the thermodynamic factor for diffusion in f.c.c. and b.c.c. ordering systems, Acta Mater. 46 (1998) 4219–4231, https://doi.org/10.1016/S1359-6454(98)00096-2.
[67] J.L. Murray, The Al-Cr (aluminum-chromium) system, J. Phase Equilib. 19 (1998) 367, https://doi.org/10.1007/BF02735058.
[68] T. Helander, O. Tolochko, An experimental investigation of possible B2-ordering in the Al-Cr system, J. Phase Equilib. 20 (1999) 57, https://doi.org/10.1361/105497199770335947.
[69] G. Raynor, V. Rivlin, H. Baker (Ed.), ASM Handbook: Volume 3: Alloy Phase Diagrams, ASM International, Materials Park, OH, 1992.
[70] S.F. Pugh, XCII. Relations between the elastic moduli and the plastic properties of polycrystalline pure metals, Philos. Mag. 45 (1954) 823–843, https://doi.org/10.1080/14786440808520496.
[71] J. Cohron, Y. Lin, R. Zee, E. George, Room-temperature mechanical behavior of FeAl: effects of stoichiometry, environment, and boron addition, Acta Mater. 46 (1998) 6245–6256, https://doi.org/10.1016/S1359-6454(98)00254-7.